J. Comput. Appl. Res. Mech. Eng. Vol. 10. No. 2, pp. 345-359, 2021 *DOI: 10.22061/jcarme.2020.4854.1594*

Journal of Computational and Applied Research in Mechanical Engineering
jcarme.sru.ac.ir
SRTTU
JCARME
ISSN: 2228-7922

Research paper

Numerical analysis of microchannel based bio-inspired heat sinks with multiple inlet-outlet pairs for cooling square shaped circuits

K. Kandassamy[a,*] and B. Prabu[b]

[a]*Department of Mechanical Engineering, Annamalai University, Chidambaram, Tamilnadu, 608002, India*
[b]*Department of Mechanical Engineering, Pondicherry Engineering College, Puducherry, 605014, India*

Article info:

Article history:

Received: 19/02/2019
Revised: 17/04/2020
Accepted: 19/04/2020
Online: 21/04/2020

Keywords:

Micro-channel,
Heat sink,
Thermal resistance,
Hydraulic resistance,
Reynolds number.

***Corresponding author:**
kandassamy007@gmail.com

Abstract

Heat dissipation in electronic circuits is important to maintain their reliability and functionality. In this work, microchannel based bio-inspired flow field models are proposed and numerically analyzed. The proposed flow fields have single to four inlet-outlet pairs. COMSOL is used to do the numerical analysis. Conjugate heat transfer analysis is done on the quarter sectional models, utilizing bi-axial symmetry of the flow fields to reduce computational cost. Constant heat flux is applied to the base of the proposed heat sinks. The results show that the thermal and hydraulic resistances of the proposed models are lower than traditional micro-channel arrayed heat sinks. The four inlet-outlet pairs model shows a thermal resistance of 0.121 to 0.158 C/W at constant Re inlet condition, achieved with a pumping power of 0.102-0.126W. Two and four inlet-outlet pair models with aspect ratio 8.6 have a thermal resistance of 0.069 and 0.067 C/W, for pumping powers 2.078 and 4.365 W respectively. The pressure drop of the proposed models is lower than the conventional microchannel arrays.

1. Introduction

Electronic cooling devices are required to evacuate heat fluxes in the range 1-10MW/m^2. As the number of transistors per unit area increases, heat dissipation rate also increases. Straight micro channels incur high parasitic power consumption due to higher ΔP incurred for the power dissipated [1]. Most of the coolants used are air and water [2]. Recently refrigerants and nanofluids have been used in some of the experimental works on heat sinking [3-4]. Many researchers have found very high heat transfer coefficients (h) near entrance regions and reduced values nearer to exits [5-6]. The value of 'h' can be increased considerably if the boundary layers are destroyed and reattached continuously, which can be done by the usage of pin fins [7], corrugations [8], varying D_{hy} [5, 9], multistage bifurcations or connectivity between microchannels [10–13]. To accommodate high heat fluxes, larger mass flow rates of coolants are

needed to increase ΔP and pump power. Single phase flow is considered in this paper, as two-phase flow suffers from flow instabilities and pressure fluctuations due to the compressible nature of the vapour formed [14]. Manifold micro-channel heat sinks are claimed to have achieved reduction in ΔP, while achieving higher Nu when compared to microchannel heat sinks. The short path taken by the fluid flow in the microchannel heat sinks maintains flow in the development region, which increases 'h' and reduces ΔP. Split-flow arrangement is recommended in Ref [14] for reduction in flow length, ΔP reduction and 'h' increase in thermally developing flows. Researchers have done work on improvement obtained by bio-inspired flows over conventional ones in the field of fuel cells [15–22]. Research done in the area of heat sinking is focused on the variation in flow channel shapes (triangular, trapezoidal, rectangular, y-shaped) [23], cross linked channels, path length optimization [24], non-conventional flow patterns [25], channel branching angles [26], aspect ratio variation [27-28], and variable fin density [29]. Optimum α recommended in Ref [27] is 8.8-11.4. Most bio-inspired flows encountered in literature were applied to fuel cells [15–22] and constructal flow fields were applied to heat-sinking applications in references [10–13, 23-26].

1.2 Review of bio-inspired flows

Biological flows are happening in nature by branching, with reduction in branch diameters from inlet to the outlet. The leaf like flow patterns are used in bio-inspired applications as they give uniformity in species and velocity distribution in fuel cells [15–22]. Farzaneh et al [10] using a square-shaped heat sink flow-fields based on the constructal theory, claim to achieve a temperature reduction of 10-20% and ΔP of 25 to 33% compared to flow-field without branches. Manso et al [18] have concluded that reduced flow length and multiple channels with large aspect ratios give good reactant distribution in fuel cells. Lung and leaf inspired models used in fuel cells show a significant reduction in ΔP, compared to serpentine and inter-digitated flow fields [21]. The flow collecting channels in this work has a gradual increase in cross section which reduces their R_{hy} as they collect hot fluid from the smaller channels. The supply and collecting duct dimensions are similar and their converging and diverging angles are determined by trial and error method to minimize base surface temperature. The reduction in main channel cross section increases R_{hy} forcing the fluid in low resistance branching channels giving a uniform velocity field. Murray's laws of biological branching were used as an inspiration without using actual values, as the branching the length and widths of the channel must be adjusted which complicates the comparison, design and manufacturing. This numerical analysis is done to evaluate the proposed flow fields in heat sinking in square shaped electronic circuits, which is different from the general usage of these flow fields in fuel cell applications. A comparison of performance with literature is given before the conclusion. The selected parameters for analysis are overall pressure drop, Uniform surface temperature of chip (USTC), R_{hy} and R_{th}.

2. Numerical approach

For the proposed bio-inspired models the basic package dimensions are fixed from reference [7], which gives the area of $1.6^{\times}10^{-4}$ m^2. The channel width of individual microchannel is fixed at 50 and 100 μm for aspect ratio 4.3 and 8.6 respectively keeping the height of microchannel fixed at 430 μm. The inlet and outlet manifold dimensions are fixed by trial and error for achieving a lower maximum base temperature. The Re range at inlet manifold is selected to achieve a higher flow velocity at inlet to the individual microchannels in the arrays.

2.1. BC's adopted and assumptions followed

The following assumptions are used in simulation [7]:

(1) Laminar, incompressible, steady, single phase flow,
(2) Temperature effect on buoyancy forces is taken for study.
(3) External surfaces outside the heat sink are adiabatic except bottom plate, where a heat flux is applied.
(4) Total heat transfer to the fluid is the sum of convective heat to fluid from base plate and lateral surfaces of fins.

(5) The Re at inlet of the flow fields are changed by changing velocities at all inlets.
(6) Zero pressure condition is maintained at all outlets.
(7) In the present work, fluid temperature is assumed as 303K.

2.2. Geometric and operating details

The general schematic, and operating details are given in F. 1. A silicon wafer of 500µm thickness can provide the required space to etch the heat sink channels of the height 430µm. Models are analyzed at two different inlet conditions namely, constant Re (maintained at 2300) [7] and constant pressure inlet of 206.84 kPa [30]. The effect of α, ε on R_{th}, R_{hy} is studied by this procedure. The materials used in all the models are water, Silicon, and PDMS. All material properties are referred from reference [7] and the same is used in the proposed models. The models are developed on a X-Y plane by extruding in the Z direction as shown in Fig. 1.

2.3. Mathematical models adopted and data reduction

The mathematical differential equations applicable to the proposed models are given in reference [31]. The continuity and momentum are given by Eq. (1-2),

$$\rho\nabla\cdot(u)=0 \quad (1)$$

$$\rho(u.\nabla)u=\nabla\cdot[-pI+\mu(\nabla u+(\nabla u)^T)]+F \quad (2)$$

$$F=-g*\Delta\rho \quad (3)$$

Eq. (3) gives the source term corresponding to body force F and Δρ- indicates change in mass density caused by thermal heating. The fluid and solid energy equations are computed using Eqs. (4-5).

$$\rho C_P u\cdot\nabla T+\nabla\cdot q=Q \quad (4)$$

Q is the heat supplied per unit volume (W/m^3). The conduction Eq. (5) is applicable to the entire domain. The inlet averaged Nu and Re_{ch} are obtained from Eqs. (6-7) using $D_{hy\text{-}in}$ and $D_{hy\text{-}ch}$ respectively.

$$q=-k\nabla T \quad (5)$$

$$Nu=\frac{h_{avg}D_{hy\text{-}in}}{k_f} \quad (6)$$

The Channel Re is calculated by evaluating the average velocity and kinematic viscosity from the simulation results at mid-channel height (in the Z axis direction) and multiplying with $D_{hy\text{-}ch}$. The Re_{in}, R_{th} and R_{hy} for the models are calculated using Eqs. (7-11). In Eq. (8), T_{max} is the maximum fin base temperature at outlet and T_{min} is the inlet coolant temperature. The inlet averaged overall h is calculated using Eq. (12).

$$Re_{in}=\frac{\rho u D_{hy\text{-}ch}}{\mu} \quad (7)$$

$$R_{th}=\frac{T_{max}-T_{min}}{Q_{th}} \quad (8)$$

$$Q_{th}=q_b*A_b \quad (9)$$

$$R_{hy}=\frac{P}{Q_{hy}} \quad (10)$$

$$Q_{hy}=n*u_{in}*A_{in} \quad (11)$$

$$h_{avg}=\frac{q_b}{T_{max}-T_{min}}\ W/(m^2K) \quad (12)$$

Table 1. Results of convergence study at Re 2300 and α- 4.3, for different flow fields taken for study.

Model	No of elements ×10^6	T_{max}	$\Delta P_{avg\text{-}in}$ kPa	$\frac{T_i-T_{i-1}}{T_i}$ ×100	$\frac{P_i-P_{i-1}}{P_i}$ ×100
SI-m	0.28	328.1	17.70		
	0.41	328.3	17.29	0.07	-2.37
	1.42	328.9	17.29	0.18	0.023
SI	0.27	330.3	18.21		
	0.44	331.9	17.76	0.50	-2.53
	0.79	333.2	17.71	0.36	-0.26
DI	0.28	318.5	13.56		
	0.72	319.9	13.36	0.41	-1.45
	1.29	320.1	13.38	0.07	0.12
FI	1.00	314.7	16.88		
	2.25	315.1	17.65	0.15	4.32
	6.84	315.7	17.74	0.17	0.52

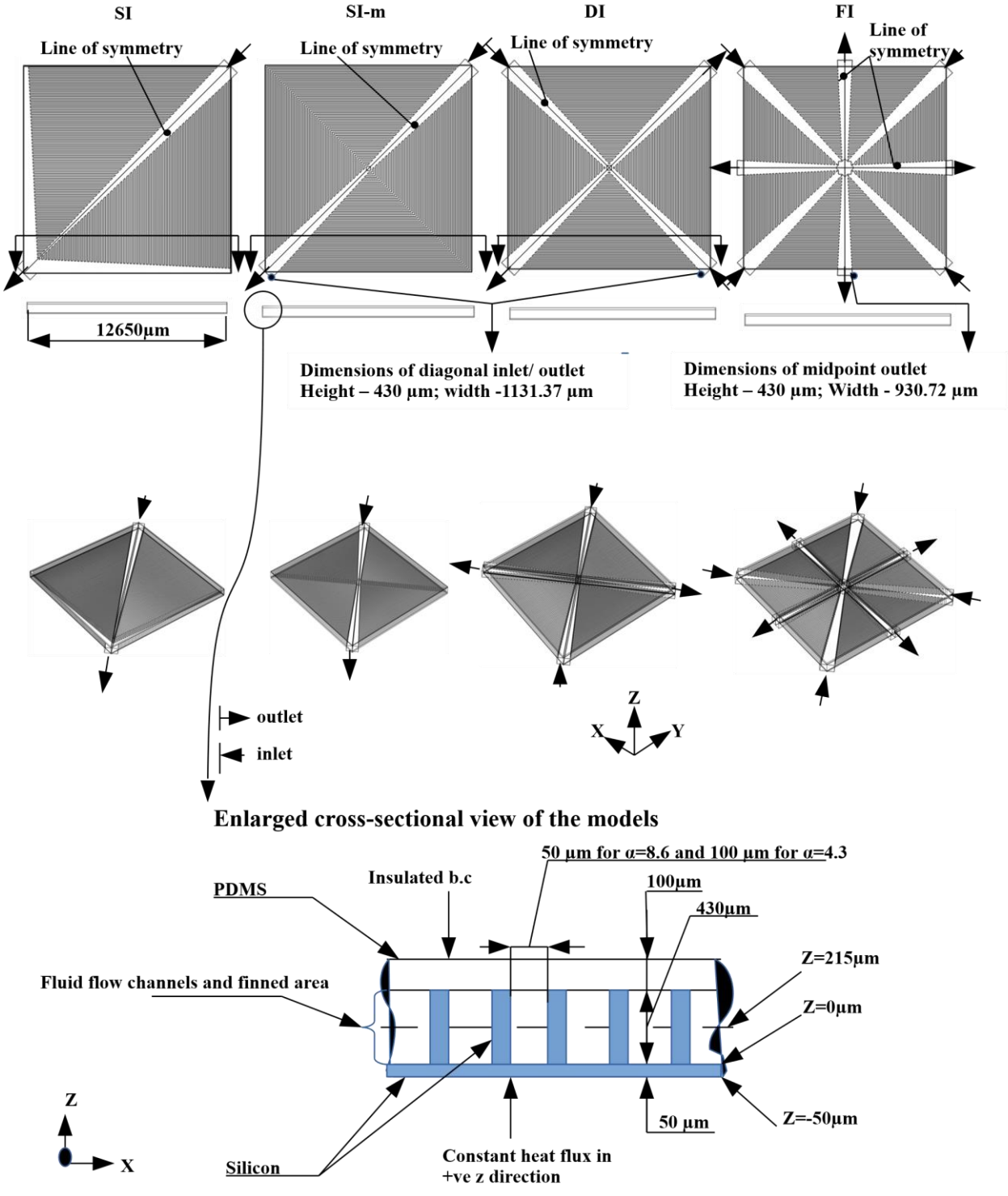

Fig. 1. Basic model dimensions taken for study.

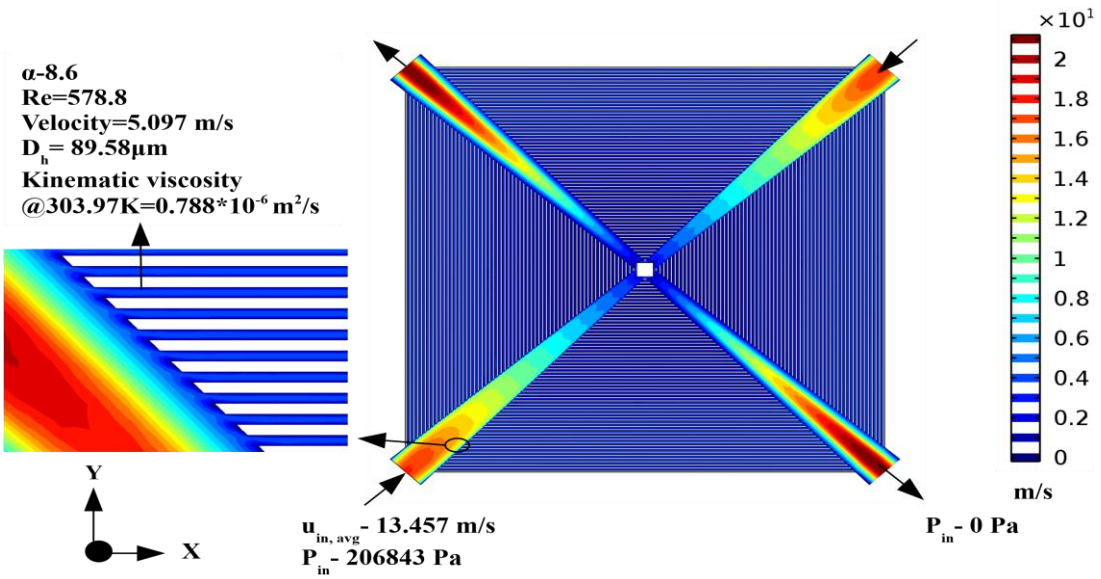

Fig. 2. Velocity field at mid-channel height for secondary channel velocity calculation.

where q_b is the base heat flux (W/m^2). Total magnitude of heat flux is the sum of local heat conduction and convection. The porosity(ε), USTC and W_p are calculated using Eqs. (14-15).

$$\varepsilon = \frac{\text{Volume of voids}}{\text{Total volume of heat sink}} \quad (13)$$

$$\text{USTC}\,\% = \frac{T_{\max} - T_{\min}}{T_{\text{avg}}} * 100 \quad (14)$$

$$W_p = n * u_{\text{in}} * A_{\text{in}} * \Delta p_{avg} \quad (15)$$

'n' is the number of inlet-outlet pairs in the model. A numerical performance index PF is defined similar to references [25, 29], as the ratio of heatsinking to the W_p, Eq. (16). A design with a higher PF can dissipate more heat at a given W_p. The temperature difference is included to factor in its non-uniformity. The Po number for the proposed models is calculated using the correlation developed by Shah and London as given in Eq. (17). fr is evaluated using Eq. (18).

$$PF = \frac{Q_{th}}{(T_{b,max} - T_{b,min}) * W_p} \quad (16)$$

$$Po = 24\left(1 - \frac{1.3553}{\alpha} + \frac{1.9467}{\alpha^2} - \frac{1.7012}{\alpha^3} + \frac{0.9564}{\alpha^4} - \frac{0.2537}{\alpha^5}\right) \quad (17)$$

$$fr = \frac{Po}{\text{Re}_{ch}} \quad (18)$$

2.4. Numerical analysis

Computation is done on a desktop computer using i7 processor with 64GB in-built RAM. 3D quarter section models based on bi-axial symmetry are solved with increasing mesh densities. A sample velocity field for Re_{ch} calculation is given in Fig. 2. The simulation results analyzed using, fin base temperature of the flow field, Fig. 3, the velocity magnitude, Fig. 4, pressure contours at mid-channel height, Fig. 5, and total heat flux at fin base, Fig. 6, for the proposed models that are presented. Convergence study is conducted by increasing the mesh density and calculating the temperature and pressure change variation percentages by comparison with the previous iterations. All the results show convergence with relative error percentages below 1%, Table 1.

3. Results and discussion

3.1. Validation

A detailed numerical procedure validation done by the present authors is given in [7] which is comparable and relevant to this work; hence

separate procedural validation is not presented here. As the proposed heat sinks are novel, similar works to be used as reference benchmarks are currently unavailable in the literature. Hence the validation of the present work is done by energy balance method.

$$\rho_f * u_{\text{in}} * A_{\text{in}} * C_{pf} * \left(T_{\text{avg-out-theo}} - T_{\text{avg-in}}\right) = Q_{th} \quad (19)$$

$T_{avg,in}$ is 303K and $T_{avg\text{-}out\text{-}theo}$ is calculated. The C_{pf} value is assumed as - 4.18 KJ/kg K in the operating conditions. The mixing cup outlet temperature obtained by simulation ($T_{avg\text{-}out\text{-}act}$) is presented in Eq. (20). The comparison between the derived value ($T_{avg\text{-}out\text{-}theo}$) and the mixing cup outlet temperature ($T_{avg\text{-}out\text{-}act}$) is shown in Table 2, the relative error is less than 1%.

$$T_{\text{avg-out-simulation}} = \frac{\int_A Tu\cdot\hat{n}dA}{\int_A u\cdot\hat{n}dA} \quad (20)$$

where, u- velocity is perpendicular to the outlet plane; T -Temperature; n- normal vector; A-Area.

3.2. Temperature Profile

The proposed models can be differentiated as single, two and four inlet-outlet pairs. Multiple inlet models show peak temperature reduction at all velocity conditions. The order of increasing maximum temperature at constant inlet velocity condition is as follows: FI< DI< SI-m< SI, Table 3. Higher fluid flow and lower porosity reduce the temperature variation. The inlet and outlet manifold dimensions are fixed by trial and error for achieving a lower maximum base temperature. The Re range at inlet manifold is selected to achieve a higher flow velocity at inlet of the individual microchannels in the arrays.

3.3. USTC

USTC decreases with decreasing porosity, increasing aspect ratio and inlet pressure (due to area increase), Table 3. An increase in number of inlets decreases USTC value, due to increase in coolant flow rate for all analyzed models. The lowest USTC obtained in this work is 1.65% for the FI model. Reasons for variation in USTC are (i) large differences in heat flux (ii) heat spreading technique, which uses a larger finned base area in comparison to heat source area and utilizing higher thermal conductivity materials.

3.4. Thermal resistance (R_{th})

R_{th} is used for comparing heat transfer characteristics of heat sinks, Table 4. At a model inlet Re of 2300 the highest R_{th} is for SI-0.393 C/W and the lowest is for the FI model-0.121 C/W, Fig. 7(d). For models with lower α, the flow non uniformity at model corners, and for models with higher α, insufficient flow velocity in channels due to higher R_{hy} increases R_{th}, Fig. 3.

Table 2. Heat balance validation of heat sinks models at constant inlet Re (2300).

Model	$Q_{in,}$	$T_{surf\text{-}avg,\ out,theo}$	$T_{surf\text{-}avg,\ out,\ act}$	Relative Error %
SI-m	80	317.07	318.61	-0.48
SI	80	317.07	317.73	-0.21
DI	80	310.04	310.29	-0.08
FI	80	306.52	306.31	0.07

Table 3. Results of USTC% at Re-2300 for various flow fields studied.

Model	α	ε	ΔP	T_{max}	T_{min}	T_{avg}	USTC
SI^v	8.6	0.57	23.43	334.5	303.3	315.4	9.88
$S\text{-}m^v$	8.6	0.53	36.96	332.7	303.7	312.6	9.51
SI^v	4.3	0.57	17.71	333.2	303.4	317.2	9.37
$SI\text{-}m^v$	4.3	0.53	17.29	328.8	303.4	315.6	8.05
DI^v	8.6	0.57	22.23	319.9	303.9	311.4	5.13
DI^v	4.3	0.57	13.38	320.0	304.61	311.5	4.96
SI^p	8.6	0.57	206.84	315.4	303.25	307.9	3.96
SI^p	4.3	0.57	206.84	315.0	303.2	309.1	3.80
FI^v	4.3	0.62	17.74	315.7	305.5	310.0	3.26
FI^v	8.6	0.61	21.85	312.7	303.5	307.7	2.97
$SI\text{-}m^p$	8.6	0.53	206.84	311.9	303.2	307.2	2.82
FI^p	4.3	0.62	206.84	311.5	303.5	306.9	2.62
$SI\text{-}m^p$	4.3	0.53	206.84	309.6	303.2	307.3	2.05
DI^p	4.3	0.57	206.84	309.3	303.3	306.2	1.96
DI^p	8.6	0.57	206.84	308.5	303.4	304.6	1.67
FI^p	8.6	0.61	206.84	308.3	303.3	305.5	1.65

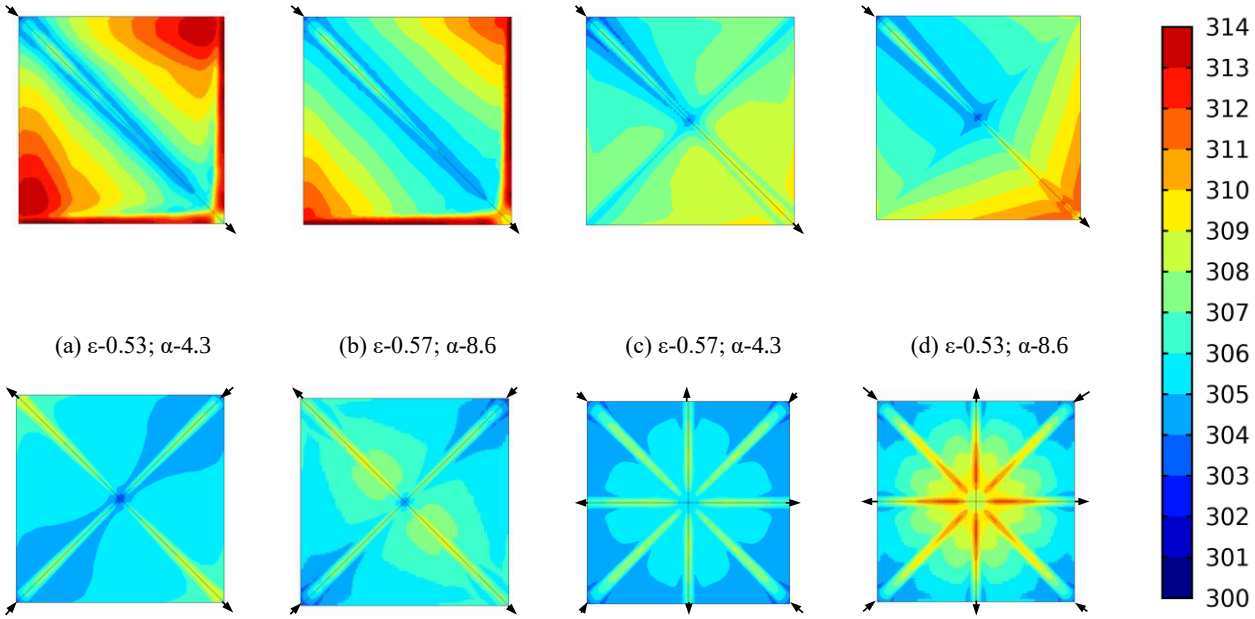

(a) ε-0.53; α-4.3 (b) ε-0.57; α-8.6 (c) ε-0.57; α-4.3 (d) ε-0.53; α-8.6

(e)ε-0.57; α-8.6 (f) ε-0.57; α-4.3 (g) ε-0.61; α-8.6 (h) ε-0.62; α-4.3

Fig. 3. Base temperature of heat sinks for constant inlet Re and pressure in x-y plane (a-b) SI; (c-d) SI-m; (e-f) DI; (g-h) FI.

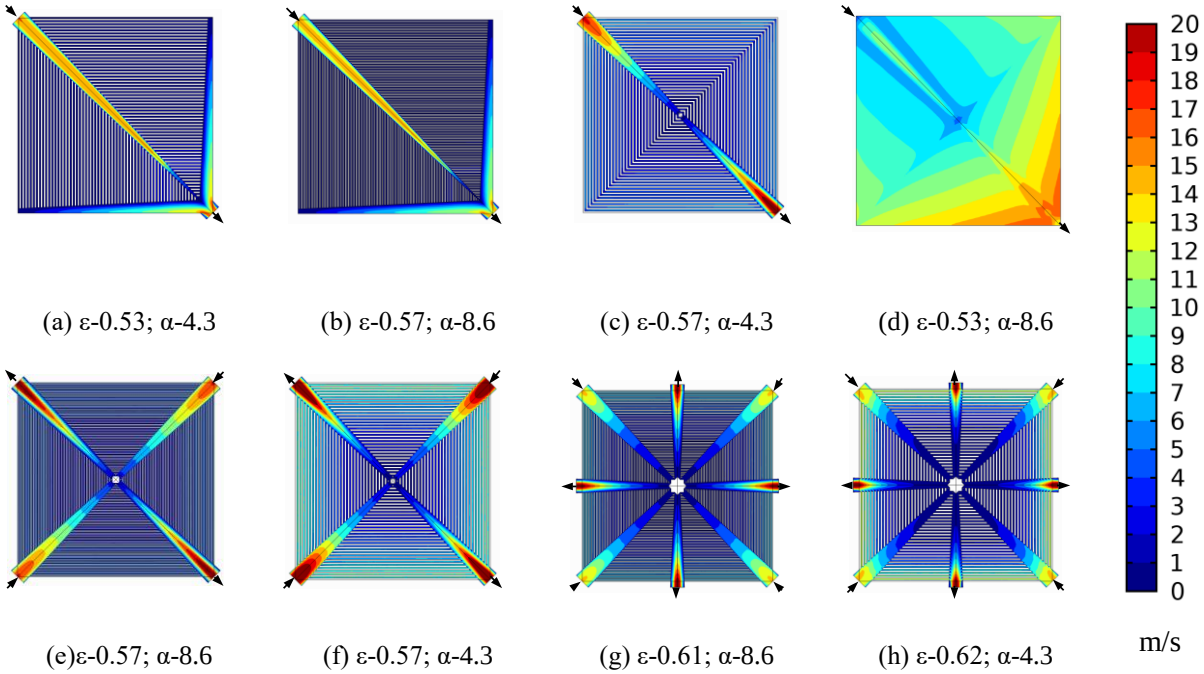

(a) ε-0.53; α-4.3 (b) ε-0.57; α-8.6 (c) ε-0.57; α-4.3 (d) ε-0.53; α-8.6

(e)ε-0.57; α-8.6 (f) ε-0.57; α-4.3 (g) ε-0.61; α-8.6 (h) ε-0.62; α-4.3

Fig. 4. Velocity magnitude of fluid at mid-channel height for constant inlet Re and pressure in x-y plane (a-b) SI; (c-d) SI-m; (e-f) DI; (g-h) FI.

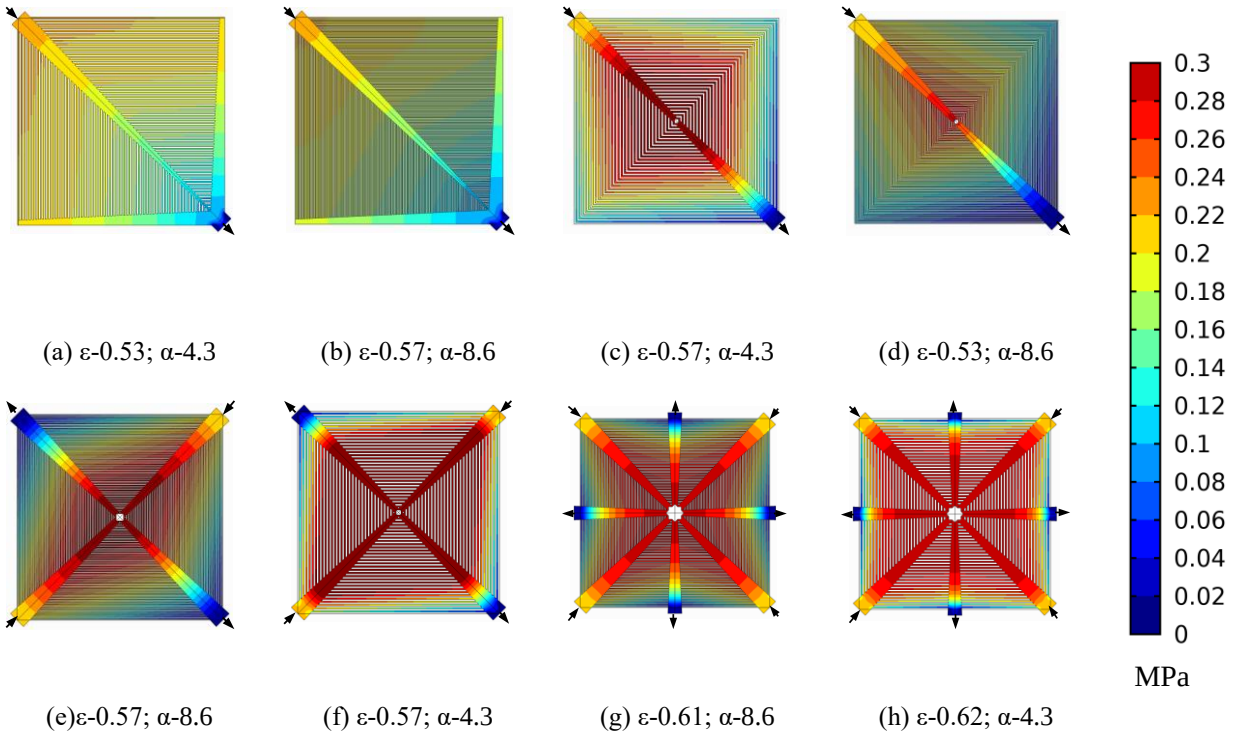

Fig. 5. Pressure contours at mid-channel height for constant inlet Re and pressure (a-b) SI; (c-d) SI-m; (e-f) DI; (g-h) FI.

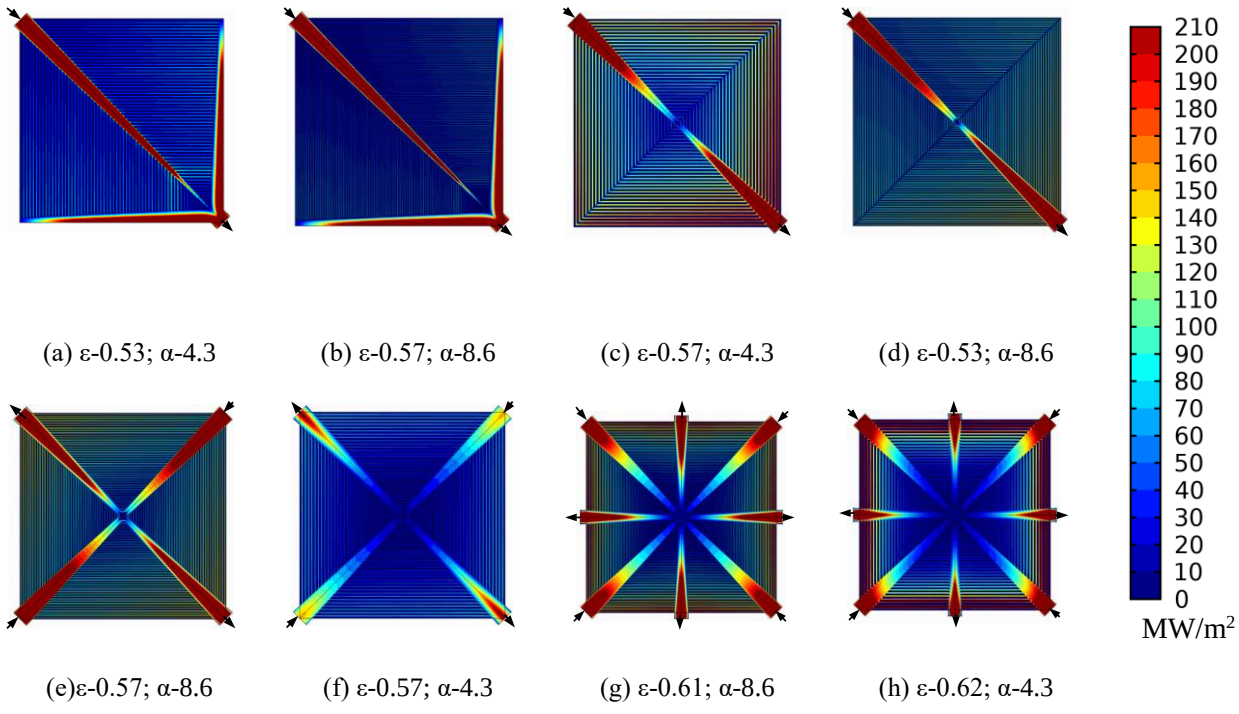

Fig. 6. Total heat flux contours at mid-channel height for constant inlet Re and pressure (a-b) SI; (c-d) SI-m; (e-f) DI; (g-h) FI.

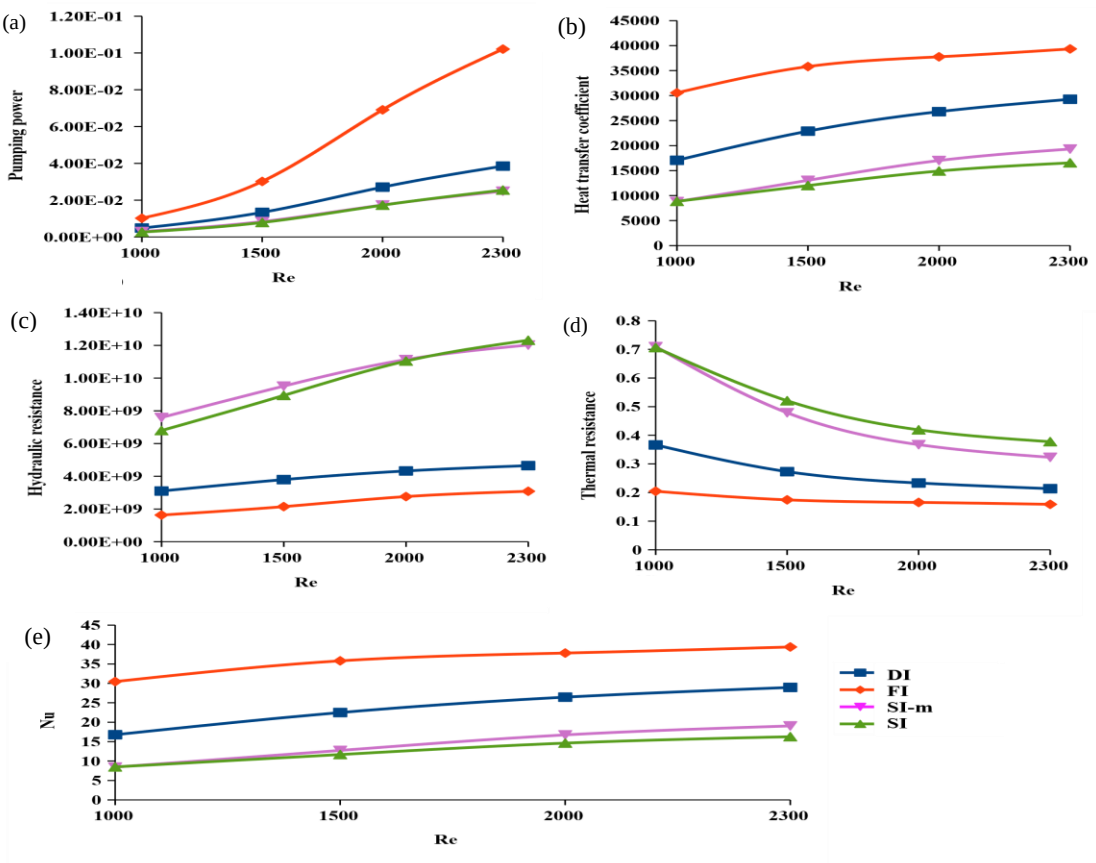

Fig. 7. Variation of (a) W_p in W, (b) overall h in W/m^2K, (c) R_{hy} in Pa. s/m^3, (d) R_{th} in C/W, and (e) Nu with Re_{in}.

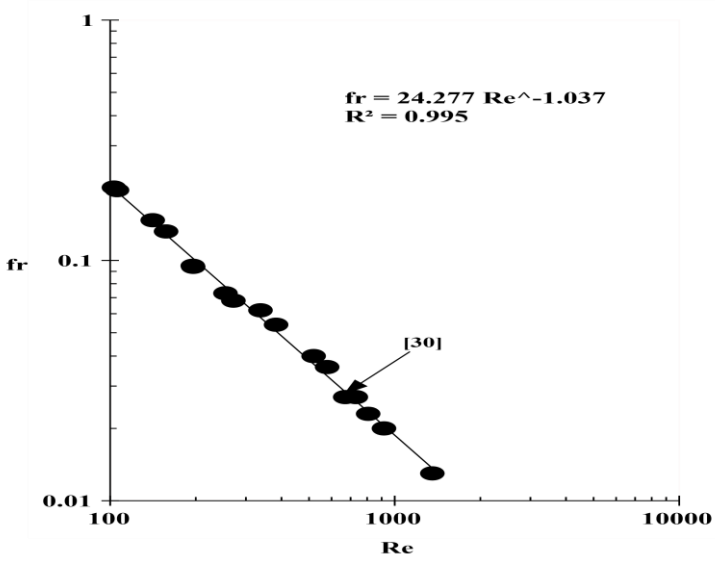

Fig. 8. Effect of channel Re on fr, for the analyzed flow-field models, plotted from data in Table 6.

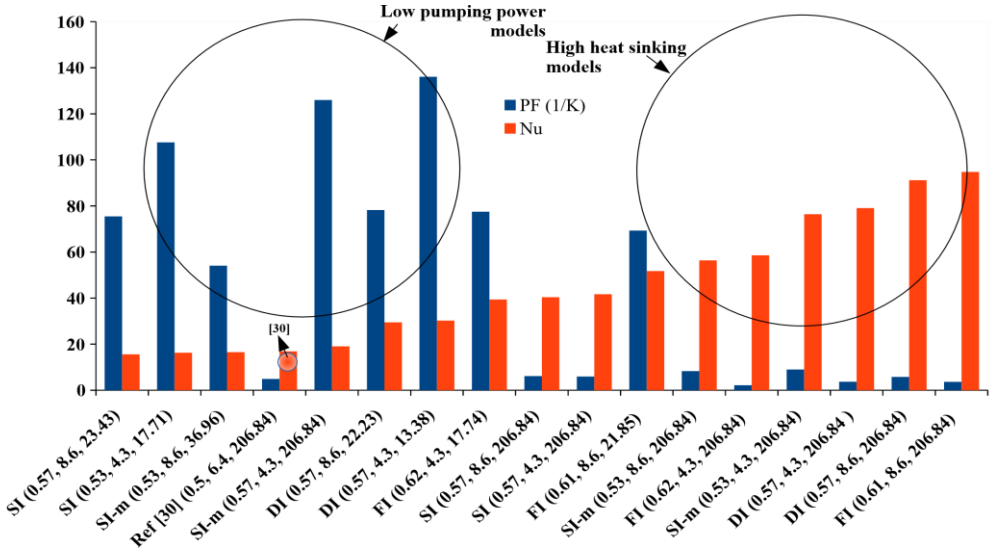

Fig. 9. Variation of PF and inlet averaged Nu for flow fields with variables (ε, α and ΔP).

This is overcome in multiple inlet models by the inclusion of inlets-outlet pairs at the diagonal corners. For comparison with Ref [30], all models are tested at an inlet pressure of 206.84 KPa and the FI model achieved a R_{th} of 0.0672 C/W, a reduction of 25.16% from the reference. The FI models show a 2.9% variation in R_{th} compared to DI models with a 38% increase in W_p as shown in Tables 4 and 5. The shorter fluid flow channel lengths and higher flow rates of FI in comparison to SI models for a given ΔP and α are the main reasons for lower R_{th} and R_{hy} of these models, as shown in Figs. 3- 4, [32]

3.5. Heat transfer coefficient (h)

Fully developed flows have little variation of h with change in Re. The model ordering based on 'h' at constant inlet Re is SI<SI-m<DI<FI, Fig. 7(b). In this work periodic changes in boundary layer condition contributes to higher h, than other comparable flow fields, Table 6. For single channel flows, h decreases in the flow direction with maximum values occurring at inlets because of thinning and subsequent thickening of boundary layer in the flow direction, reducing the temperature gradient. Advantage of split-flow arrangement is due to this entrance effect. The destruction of boundary layers at inlet and re-attachment at the outlet manifolds maintains the flow as a developing one throughout the device. The higher temperature gradient available due to fluid mixing is favorable for heat transfer. The h for all models increases with Re. The local heat flux contours show a smooth variation for flow field models with higher α, Fig. 6. The temperature contours show higher local heat fluxes in the convergent and divergent ducts because of conjugate heat conduction in the silicon substrate from regions of higher convection resistance to regions with lower ones, Ref [33]. This effect is visualized in Fig. 6. According to the experimental work in Ref [34], wall conduction in plain converging microchannels is larger, due to higher temperature gradient than divergent microchannels with lower gradients. But in this work, divergent duct shows higher heat fluxes as the boundary layer in the convergent ducts is sucked into flow inlets of the branching channels while the boundary layer thickness gradually increases in the outlet diverging ducts, with fluid mixing confined to the central regions of the diverging ducts.

3.6. Nusselt number (Nu)

Nu increases with microchannel and flow field inlet Re as shown in Fig. 7(e). An increase in aspect ratio also increases inlet averaged Nu, Table 5. Chen et al have shown that for microchannel flows overall Nu is a function of ε

and α. Inlet averaged Nu number decreases as porosity increases. Nu increases for higher values of ε at constant α [35]. The overall Nu increases with aspect ratio and inlet pressure. The Nu values for both constant velocity and pressure inlet conditions are shown in Table 5.

3.7. Pressure drop (ΔP)

ΔP across flow fields with higher aspect ratio is gradual than the lower aspect ratio models, Fig. 5. The lower α models have ΔP below 40 kPa for constant inlet velocity conditions. As the inlet pressure is increased at constant porosity and aspect ratios, the pressure gradient increases proportionately across the entire flow fields for all the analyzed models. The DI model has the lowest ΔP among all the models tested at α's-4.3 and 8.6 for constant inlet Re-2300 of the models. Higher α contributed to higher ΔP. Pressure increases in the inlet manifolds towards the central region of all the heat sink models due to stagnation pressure rise (higher pressure than inlet in the central region) and in the outlet manifolds the pressure reduction is gradual due to the diverging duct which increases pressure and the rejoining of fluid streams at different locations. The α and ε are two factors that influence pressure drop, among these α has higher influence as seen in Table 5. The proposed models having, secondary channel width of 50 µm are tested with inlet pressures 206.84 kPa as in reference [30]. For a channel D_{hy} -89.6 µm the maximum Re in the secondary channel for an inlet manifold ΔP of 206.84 kPa is 1356, which is in the laminar flow regime, as shown in Fig. 2. Higher channel Re values are obtained for DI model at α-4.3. For the same α, reduction in ε increases heat transfer and ΔP. The results are summarized in Table 5.

3.8. Hydraulic resistance (R_{hy})

R_{hy} is analogous to electrical resistance offered by a circuit to current flow for an applied voltage, in the present case fluid flow rate for an applied pressure drop, Table 5. Comparisons between heat sinks are possible using R_{hy}. The FI model has the lowest R_{hy} among all the analyzed models due to the higher flow rates for a given pressure drop. The order of R_{hy} at Re-2300 is FI<DI<SI-m<SI as shown in Fig. 7(c). The lowest value of R_{hy} - $9.8^{\times}10^{9}$ Pa.s/m^3 at α- 8.6 and R_{hy}- $3.08^{\times}10^{9}$ Pa.s/m^3 at α- 4.3 are obtained for FI model at constant inlet pressure and Re conditions respectively. The lowest R_{hy} of this model is due to short path length traveled by the fluid between any inlet and two adjacent outlets. A chart showing the variation of channel fr of all models analyzed in this work with respect to channel Re's is given in Fig. 8. It indicates the laminar nature of the flows analyzed. Models with α-8.6 show more flow uniformity than ones with α-4.3. The uniformity of flow in the models is highlighted in Fig. 2 and 4.

3.9. Pumping power (W_p)

Pumping power increases in the following order for the models at constant inlet Re: SI<SI-m<DI<FI, Fig. 7(a) and Table 5. Higher α correlates to a higher ΔP and W_p. Effect of variation of ε is studied at two α levels - 4.3 and 8.6 in this work. As branching increases, ΔP increases due to an increase in the surface area, but shorter path lengths negate these effects.

Table 4. Results of R_{th} and R_{hy} for various flow fields studied at Re 2300 and $D_{hy\text{-}in}$=623.1µm**.**

Model	ε	α	$D_{hy\text{-}ch}{}^{c}$	ΔP	R_{th}	R_{hy} ×10^9
SI^{v}	0.57	8.6	89.5	23.43	0.393	16.3
SI^{v}	0.53	4.3	162.2	17.71	0.377	12.3
SI-m^{v}	0.53	8.6	89.5	36.96	0.372	26.6
SI-m^{v}	0.57	4.3	162.2	17.29	0.323	12.0
DI^{v}	0.57	8.6	89.5	22.23	0.211	7.72
DI^{v}	0.57	4.3	162.2	13.38	0.204	4.71
FI^{v}	0.62	4.3	162.2	17.74	0.158	3.08
SI^{p}	0.57	8.6	89.5	206.84	0.155	39.9
SI^{p}	0.57	4.3	162.2	206.84	0.150	37.2
FI^{v}	0.61	8.6	89.5	21.85	0.121	3.79
SI-m^{p}	0.53	8.6	89.5	206.84	0.112	38.5
FI^{p}	0.62	4.3	162.2	206.84	0.107	9.38
[30]	0.50	6.4	98.6	206.84	0.089	18.8
SI-m^{p}	0.53	4.3	162.2	206.84	0.082	30.4
DI^{p}	0.57	4.3	162.2	206.84	0.079	11.8
DI^{p}	0.57	8.6	89.5	206.84	0.069	15.8
FI^{p}	0.61	8.6	89.5	206.84	0.067	9.80

This is the reason for higher pumping power requirement for the FI compared to the DI model at α-4.3. The convergent inlets and divergent outlets improve pressure recovery. A comparison of the proposed models based on PF and inlet averaged Nu data of models analyzed in this work is shown in Fig. 9.

3.10. Effect of porosity (ε)

No particular effort was made to vary the porosity and the porosity is a consequence of tweaking the models to achieve minimum base temperature. The results are tabulated and the effects of porosity on the results are analyzed here. For each aspect ratio, there exists an optimum porosity, any further change in **ε** decreases Nu [35]. A decrease in ε increases ΔP, surface area, friction and heat transfer. Interpolation from Ref [35] yields a Nu value of 16 and 180 for α-1.54 and 8.6 respectively. Similarly, the optimum ε for α's mentioned above are 0.85 and 0.5 respectively. For constant ε, a Re increase causes ΔP, R_{hy}, Nu and pumping power to increase, while R_{th} decreases.

Table 5. Results of W_p and Nu for the proposed heat sinks evaluated at inlet diameter.

Model	ε	α	Re^c	fr	W_p	PF	Nu_{avg}
SI[v]	0.57	8.6	103.1	0.201	0.034	75.5	15.58
SI[v]	0.53	4.3	195.8	0.094	0.025	107.6	16.27
SI-m[v]	0.53	8.6	105.7	0.196	0.051	54.1	16.52
[30][p]	0.50	6.4	730	0.027	2.275	4.9	16.88
SI-m[v]	0.57	4.3	195.2	0.095	0.024	125.9	19.04
DI[v]	0.57	8.6	141.1	0.147	0.064	78.2	29.47
DI[v]	0.57	4.3	254.2	0.073	0.038	136.1	30.23
FI[v]	0.62	4.3	271.1	0.068	0.102	77.5	39.37
SI[p]	0.57	8.6	337.5	0.062	1.069	6.1	40.37
SI[p]	0.57	4.3	670.1	0.027	1.147	5.9	41.67
FI[v]	0.61	8.6	157.2	0.132	0.126	69.3	51.73
SI-m[p]	0.53	8.6	382.9	0.054	1.111	8.3	56.36
FI[p]	0.62	4.3	916.8	0.020	4.562	2.17	58.56
SI-m[p]	0.53	4.3	806.8	0.023	1.407	8.9	76.40
DI[p]	0.57	4.3	1356	0.013	3.615	3.7	79.06
DI[p]	0.57	8.6	578.8	0.036	2.708	5.8	91.16
FI[p]	0.61	8.6	518.9	0.040	4.365	3.6	94.76

Table 6. Comparison of models with published results having similar W_p.

Model	ε	α	Re^c	fr	PF	R_{th}	$h\times10^3$
[3]	0.57	3.15	250	0.071	14.76	0.153	32.50
SI	0.57	4.3	397.4	0.046	9.94	0.226	27.60
SI-m	0.57	4.3	488.2	0.038	14.20	0.162	38.44
DI	0.57	4.3	573.2	0.032	16.61	0.140	44.48
DI	0.57	8.6	253.9	0.081	14.89	0.156	39.96
FI	0.59	8.6	168.8	0.123	23.43	0.101	61.39
[36]	0.73	8.62	128.8	0.161	26.53	0.108	34.10
FI	0.59	8.6	179.4	0.116	29.41	0.105	59.45

4. Comparison with published results

The proposed flow field configurations are compared with published results in Table 6. Experimental work of Ref [3] is compared with analyzed models of this work at similar ε, W_p, fluid inlet temperature and q. All four presented models show lower ΔP than Ref [3]. Comparison with [36] is carried out with input parameters as specified in the reference work. The R_{th} of the analyzed models in this work is lower than the reference work except for the single-inlet model. One interesting feature is the higher individual microchannel Re's of the proposed models in comparison with [3, 36], except the FI model which shows a 32.44% lower value than [3].

5. Conclusions

Based on numerical evaluation, the following conclusions are arrived. The trends obtained for the proposed models show improvements that are explained below:

1. Bio-inspired pin fin models show lower R_{hy} when compared to references cited in this work, because of flow uniformity and higher fluid flow for a given ΔP across the heat sinks.
2. Proposed models have lower ΔP's at similar W_p.
3. W_p of the proposed models decreases with higher flow rates consequentially increases Nu.
4. In case of constant pressure inlet condition, the proposed FI model shows lower value of R_{th} -0.0673 C/W compared to benchmark value by 25% provided ε- 0.62 and $D_{h\text{-}ch}$ -89.6μm.

5. Models with multiple inlets give high heat transfer due to increased coolant flow rates, boundary layer thickness reduction and shorter path lengths.
6. Aspect ratio α and porosity ε are important parameters in the characterization of finned heat sinks.
7. For similar porosities, multiple flow inlets reduced the maximum base temperature and USTC %.
8. Decrease in ε increases Nu and decreases R_{th} due to higher heat transfer area.
9. For a given base area higher heat fluxes can be dissipated without phase change by the bio-inspired SI-m, DI and FI models.
10. The conclusion is that when flow-fields are designed for higher heat transfer, W_p increases and if designed for minimum W_p, lower heat transfer occurs.
11. The correlation of all the flows analyzed in this work is given as; fr $^{\times}Re^{1.037}$= 24.277 with R^2 = 0.995

References

[1] S. Lu and K. Vafai, "A comparative analysis of innovative microchannel heat sinks for electronic cooling", *Int. Commun. Heat Mass Transf*, Vol.76, No. 8, pp. 271–284, (2016).

[2] A. C. Kheirabadi and D. Groulx, "Cooling of server electronics: A design review of existing technology", *Appl. Therm. Eng*, Vol. 105, No. 7, pp. 622–638, (2016).

[3] P. Bhattacharya, A. N. Samanta, and S. Chakraborty, "Numerical study of conjugate heat transfer in rectangular microchannel heat sink with Al_2O_3/H_2O nanofluid", *Heat Mass Transf*, Vol. 45, No. 10, pp. 1323–1333, (2009).

[4] W. Duangthongsuk and S. Wongwises, "A comparison of the thermal and hydraulic performances between miniature pin fin heat sink and microchannel heat sink with zigzag flow channel together with using nanofluids", *Heat Mass Transf*, Vol. 54, No. 5, pp. 3265–3274, (2018).

[5] M. Dehghan, M. Daneshipour, M.S. Valipour, R. Rafee, S. Saedodin, "Enhancing heat transfer in microchannel heat sinks using converging flow passages", *Energy Convers. Manag*, Vol. 92, No. 3, pp. 244–250, (2015).

[6] W. Qu and I. Mudawar, "Experimental and numerical study of pressure drop and heat transfer in a single-phase micro-channel heat sink", *Int. J. Heat Mass Transf.*, Vol. 45, No. 12, pp. 2549–2565, (2002).

[7] K. Kandassamy, and B. Prabu, "Numerical Investigation of Bio-Inspired Pin Fin Heat Sink Models for Square Shaped Electronic Circuits", *J. App. Sci. and Eng.*, Vol. 22, No. 1, pp. 119–33, (2019).

[8] M. Khoshvaght-Aliabadi and F. Nozan, "Water cooled corrugated minichannel heat sink for electronic devices: Effect of corrugation shape", *Int. Commun. Heat Mass Transf*, Vol. 76, No. 8, pp. 188–196, (2016).

[9] I. Ali, N. Azwadi, C. Sidik, and N. Kamaruzaman, "International Journal of Heat and Mass Transfer Hydrothermal performance of microchannel heat sink: The effect of channel design", *Int. J. Heat Mass Transf*, Vol. 107, No. 4, pp. 21–44, (2017).

[10] M. Farzaneh, M. R. Salimpour, and M. R. Tavakoli, "Design of bifurcating microchannels with/ without loops for cooling of square-shaped electronic components", *Appl. Therm. Eng*, Vol. 108, No. 9, pp. 581–595, (2016).

[11] D. Heymann, D. Pence, and V. Narayanan, "Optimization of fractal-like branching microchannel heat sinks for single-phase flows", *Int. J. Therm. Sci*, Vol. 49, No. 8, pp. 1383–1393, (2010).

[12] G. Xie, F. Zhang, B. Sundén, and W. Zhang, "Constructal design and thermal analysis of microchannel heat sinks with multistage bifurcations in single-phase liquid flow", *Appl. Therm. Eng*, Vol. 62, No. 2, pp. 791–802, (2014).

[13] C. A. Rubio-jimenez, A. Hernandez-guerrero, J. G. Cervantes, D. Lorenzini-gutierrez, and C. U. Gonzalez-valle, "CFD study of constructal microchannel

networks for liquid-cooling of electronic devices", *Appl. Therm. Eng*, Vol. 95, pp. 374–381, (2016).

[14] S. G. Kandlikar, "High flux heat removal with microchannels - A roadmap of challenges and opportunities", Heat *Transf. Eng.*, Vol. 26, No. 8, pp. 5–14, (2005).

[15] T. Chen, Y. Xiao, and T. Chen, "The impact on PEMFC of bionic flow field with a different branch", *Energy Procedia*, Vol. 28, pp. 134–139, (2012).

[16] J. Currie, "Biomimetic design applied to the redesign of a PEM fuel cell", *M.A.Sc thesis, University of Toronto*, Canada, (2010).

[17] R. Roshandel, F. Arbabi, and G. K. Moghaddam, "Simulation of an innovative fl ow- field design based on a bio inspired pattern for PEM fuel cells", *Renew. Energy*, Vol.41, pp. 86–95, (2012).

[18] A. P. Manso, F. F. Marzo, J. Barranco, X. Garikano, and M. Garmendia Mujika, "Influence of geometric parameters of the flow fields on the performance of a PEM fuel cell. A review", *Int. J. Hydrogen Energy*, Vol. 37, No.20, pp. 15256–15287, (2012).

[19] D. Ouellette, A. Ozden, M. Ercelik, C. O. Colpan, H. Ganjehsarabi, X. Li, and F. Hamdullahpur, "Assessment of different bio-inspired flow fields for direct methanol fuel cells through 3D modeling and experimental studies", *Int. J. Hydrogen Energy*, Vol. 43, No. 2, pp. 1152–1170, (2018).

[20] A. Arvay, J. French, J. Wang, X. Peng, and A. M. Kannan, "Modeling and Simulation of Biologically Inspired Flow Field Designs for Proton Exchange Membrane Fuel Cells", *Open Electrochem. J.*, Vol. 6, pp. 1–9, (2015).

[21] P. Trogadas, J. I. S. Cho, T. P. Neville, J. Marquis, B. Wu, D. J. L. Brett, and M. O. Coppens, "A lung-inspired approach to scalable and robust fuel cell design", *Energy Environ. Sci.*, Vol. 11, No. 1, pp. 136–143, (2018).

[22] F. Arbabi, Numerical Modeling of an Innovative Bipolar Plate Design Based on the Leaf Venation Patterns for PEM Fuel Cells, *Int. J. Eng.* Vol. 25, No. 3, pp. 177–186, (2012).

[23] Y. Li, F. Zhang, B. Sunden, and G. Xie, "Laminar thermal performance of microchannel heat sinks with constructal vertical Y-shaped bifurcation plates", *Appl. Therm. Eng.*, Vol. 73, No. 1, pp. 185–195, (2014).

[24] B. Camburn, K. Otto, D. Jensen, R. Crawford, and K. Wood, "Designing biologically inspired leaf structures: computational geometric transport analysis of volume-to-point flow channels", *Eng. Comput.*, Vol. 31, No. 2, pp. 361–374, (2015).

[25] F. Cano-banda, C. U. Gonzalez-valle, S. Tarazona-cardenas, and A. Hernandez-guerrero, "Effect of different geometry flow pattern on heat sink performance", *12th Int. Con. Heat Tran., Fluid Mech. and Therm.*, Spain, pp. 419–424, (2016).

[26] X. Q. Wang, A. S. Mujumdar, and C. Yap, "Effect of bifurcation angle in tree-shaped microchannel networks", *J. Appl. Phys.*, Vol. 102, No. 7, (2007).

[27] H. Wang, Z. Chen, and J. Gao, "Influence of Geometric Parameters on Flow and Heat Transfer Performance of Micro-Channel Heat Sinks", *Appl. Therm. Eng.*, Vol. 107, pp. 870–879, (2016).

[28] C. Y. Zhao and T. J. Lu, "Analysis of microchannel heat sinks for electronics cooling", *Int. J. Heat Mass Transf.*, Vol. 45, No. 24, pp. 4857–4869, (2002).

[29] D. Lorenzini-gutierrez, "Variable Fin Density Flow Channels for Effective Cooling and Mitigation of Temperature Nonuniformity in Three-Dimensional Integrated Circuits", *J. of Electronic Packaging*, Vol. 136, No. 2, pp. 1–11, (2014).

[30] D. B. Tuckerman and R. F. W. Pease, "High-Performance Heat Sinking for VLSI", IEEE Electron Device Lett., Vol. 2, No. 5, pp. 126–129, (1981).

[31] COMSOL, "Introduction to COMSOL Multiphysics 5.3", *Manual*, (2014).

[32] D.D. Ma, G.D. Xia, J. Wang, Y.C. Yang, Y.T. Jia, L.X. Zong, "An experimental study on hydrothermal performance of microchannel heat sinks with 4-ports and offset zigzag channels", *Energy Convers. Manag*. Vol.152 pp.157–165, (2017).

[33] H. Shen, C. C. Wang, G. Xie, "A parametric study on thermal performance of microchannel heat sinks with internally vertical bifurcations in laminar liquid flow", *Int. J. Heat Mass Transf*., Vol. 117, pp. 487–497, (2018).

[34] V. S. Duryodhan, S. G. Singh, and A. Agrawal, "Heat rate distribution in converging and diverging microchannel in presence of conjugate effect", *Int. J. Heat Mass Transf*, Vol. 104, pp. 1022–1033, (2017).

[35] C. Chen, "Forced convection heat transfer in microchannel heat sinks", *Int. J. Heat Mass Transf*, Vol. 50, No. 11-12, pp. 2182–2189, (2007).

[36] G. Turkakar and T. Okutucu-ozyurt, "Dim. optimization of microchannel heat sinks with multiple heat sources", *Int. J. Therm. Sci*, Vol. 62, No. 12, pp. 85-92, (2012).

How to cite this paper:

K. Kandassamy and B. Prabu, "Numerical analysis of microchannel based bio-inspired heat sinks with multiple inlet-outlet pairs for cooling square shaped circuits,", *J. Comput. Appl. Res. Mech. Eng.*, Vol. 10, No. 2, pp. 345-359, (2021).

DOI: 10.22061/jcarme.2020.4854.1594

URL: https://jcarme.sru.ac.ir/?_action=showPDF&article=1219